Transient simulations of *large-scale* hydrogeological processes causing temperature and salinity anomalies in the Tiberias Basin

F. Magri(1,*), N. Inbar(2), C. Siebert(3), E. Rosenthal(2), J. Guttman(4) and P. Möller(1)

(1,*) GFZ German Research Centre for Geosciences, Section 5.3- Hydrogeology, Potsdam, Germany – Corresponding author: fabienma@gfz-potsdam.de
(2) Tel Aviv University, The Department of Geophysics and Planetary Sciences, Tel Aviv, Israel
(3) Helmholtz Centre for Environmental Research – UFZ, Halle, Germany
(4) Mekorot Co. Ltd., Tel Aviv, Israel

Abstract

Hot and salty waters occur in the surroundings of the Lake Tiberias. Transient numerical simulations of thermally-driven flow without salinity effects show that mixed convection can explain the upsurge of thermal waters through permeable faults and the high temperature gradient in the Lower Yarmouk Gorge (LYG). It turns out that by including salinity effects, the flow patterns differ from those of a purely thermal regime because heavy brines dampen upward buoyant flow and convective cells. Accordingly, the fault permeability had to be increased to restore a good fit with the measured temperatures. This further supports the hypothesis that the high temperature gradient in the LYG is likely due to fractures or faults in that area. The thermohaline simulations also suggest that the derivatives of relic seawater brines are the major source of salinity. Deep brines leaching salt diapirs cannot reach the surface. However, the presence of local shallower salt bodies below the lake can potentially contribute to the salinity of the western spring and well waters, though in very small amount. This is in agreement with geochemical data according to which the major source of the brines of the Tiberias basin represents seawater evaporation brines. Besides being of importance for understanding the hydrogeological processes that salinize Lake Tiberias, the presented simulations provide a real-case example illustrating large-scale fluid patterns due to only one source of buoyancy (heat) and those that are additionally coupled to salinity.

Keywords: numerical modeling; Lake Tiberias; convection; brine; fault; heat anomaly

1. Introduction

Groundwater flow, heat and brine transport processes in large-scale systems are naturally coupled and mutually dependent. Physically, the coupling is mainly through the Darcy law, in which the buoyancy forces and dynamic viscosity depend on pressure, temperature and solute concentration (e.g. Ingebristen, 1999). The consequence of this coupling is that different system behaviors arise (Chen et al. 1990). On the basis of a linear stability analysis, Lapwood (1948) shows that, for a porous medium heated from below, free convection is triggered when the value of the Rayleigh number of the medium is higher than a critical number $Ra^{critical}$. Depending on the physical properties of the fluid and geological units, different free

46 convective regimes develop in the form of thermal plumes or fingers (e.g. Nield,
47 1968). In basin systems, free convection is often related to the upsurge of hot
48 springs. For example, Severini et al. (1983) shows that convection with a normal
49 geothermal gradient is capable of producing warm springs in northwestern Virginia.
50 When dissolved solutes are also involved, mass transport within the system is
51 associated with the protrusion of the thermal plumes. In saline environments, this
52 coupled flow is called thermohaline convection. Real study cases are the salt domes
53 of the Gulf of Mexico, where upward brine flow along salt flanks occurs as the result
54 of thermohaline convection (Evans et al., 1991). In the coastal aquifers of western
55 Turkey, free convection in the faults induces seawater intrusion (Magri et al., 2012).
56 Depending on the relative importance of both sources of buoyancy (i.e. heat and
57 salt), solute can be either stabilizing and dampen thermal convection (Diersch and
58 Kolditz, 2002) or enhance gravity-driven flow, as in the case of sinking brine from
59 shallow salt structures (Sarkar et al., 1995; Magri et al., 2009).
60   When thermohaline convection interacts with the regional flow imposed by the
61 topography of the basin, the resulting flow is referred to as mixed convection. Mixed
62 convection is invoked as the main process of ore formation in the McArthur Basin,
63 Australia (Garven et al., 2001). The hydraulic conductivity of the units exerts the
64 major control on groundwater flow, and therefore strongly impacts coupled
65 processes. In this regard, permeable faults provide preferential pathways for mixed
66 convection and discharge of the regional flow. Permeable faults can even allow
67 convection within surrounding units that have a small Rayleigh number (McKibbin,
68 1986).
69   Here a numerical example illustrating the features of large-scale groundwater
70 flow coupled to heat and brine transport in a faulted system is presented. The
71 Tiberias Basin (Fig.1), in the Jordan Rift Valley serves as study case.
72   The Jordan Rift Valley is a series of rhomb-shaped pull-apart basins, one of
73 which hosts Lake Tiberias, also known as Lake Kinneret or Sea of Galilee (Fig. 1).
74 Brines are found in springs and boreholes at the shoreline of the Lake, as well as
75 seepages from the lake's floor (Fig. 1). The springs can be classified in clusters
76 according to their location and the local geological settings, as well as to their
77 chemical properties (Table 1). The lake is a major fresh water reservoir for the whole
78 area. Therefore, understanding the driving mechanisms endangering the lake is a
79 crucial aspect to manage this important freshwater resource.
80   Previous numerical simulations based on a W-E cross-section crossing the lake
81 (Gvirtzman et al., 1997a, 1997b) show that topography-driven flow from the Galilee
82 and convection below the Golan coexist (i.e. mixed convection) and can explain
83 different spring behaviors as well as the anomalous geothermal gradient of the area.
84 Similarly, Roded et al. (2013) study the high heat flow below the Lower Yarmouk
85 Gorge (LYG) along a N-S profile at the eastern side of the lake. However, those
86 studies account neither for the salinity effects of relic brines in the units nor for the
87 effects imposed by the presence of a salt dome. Furthermore, in Gvirtzman et al.
88 (1997a, 1997b) faults are not represented numerically, whereas in Roded et al.
89 (2013) the LYG sediments are strongly anisotropic with respect to the hydraulic
90 conductivity to enhance upward heat migration. The studies of Rimmer et al. (1999,
91 2003) and Abbo et al. (2003) are more conceptual: though their transient models
92 successfully explain the seasonal variability of the spring salinity and rate, they are
93 limited to a maximum depth of -900 m, and do not account for temperature effects.

94   These assumptions implicitly exclude any type of deep large-scale flow patterns and
95   source of solute below the Upper Cretaceous aquifers. Hurwtiz et al. (2000a) models
96   explain paleo temperature and the transition from a Late Pleistocene salt lake to
97   the actual fresh one. The most recent transient 3D models of Yechieli et al. (2011),
98   from the Geological Survey of Israel, investigate the effects of pumping from the
99   major aquifers on salinity and flow rates of the springs. Yechieli et al. (2011) refers
100   to Kessler's report (2011) on hydrological cells modeling and supplies different
101   forecast for salinity change as consequence of extensive pumping but does not
102   implement deep sources of the saline springs system.
103   The intention of this study is to provide a regional picture of the ongoing large-
104   scale transport processes that control the migration of relic seawater brines in the
105   Tiberias Basin and induce the high temperature anomalies. Adequate equations of
106   state (EOS) for fluid density and viscosity are implemented to account for
107   temperature and salinity dependencies. Furthermore, faults are explicitly modeled
108   using the equivalent porous media (EPM) approach to show the impact of narrow
109   permeable zones on the large-scale flow regimes and on the temperature gradient
110   of the LYG. For the first time, a salt dome based on the interpretation of actual
111   seismic lines is implemented in the numerical models. This setting allows
112   investigating whether the presence of salt structures below the lake can also
113   contribute to the salinity of the springs and wells.
114   The simulation results illustrate the calculated flow paths, as well as fluid
115   temperature and salinity patterns, supported by available temperature profiles of
116   deep wells and spring salinities. In a more general way, the presented scenarios also
117   illustrate the differences between large-scale fluid patterns due to only one source
118   of buoyancy (heat) and those that additionally combine salinity.

119   **2. Data**

120   The hydrological data available are mainly based on the yearly reports from the
121   Water Authority of Israel (2012), hydrological surveys (BGR-WAJ, 2001), geophysical
122   and numerical investigations (Yechiely et al., 2011; Kesler, 2011) and several
123   hydrochemical studies in both Israeli and Jordanian sides of the study area, as
124   recalled in this section. The data consist of interpreted geological structures,
125   regional head values, salinity, temperature and flow rates of both springs and wells.
126   They are used to define suitable boundary conditions for the numerical models as
127   well as to qualitatively calibrate the results. Isotopes provide additional constraints
128   on the possible flow paths and groundwater mixing.

129   *2.1. The selected profile and its hydrogeological setting*

130   The selected geohydrological profile starts on the western flank of the Gilboa-
131   Arbel syncline, west to the Lake Tiberias, (Fig. 1). It crosses the western side of the
132   lake, between onshore Fuliya and the offshore Ma'agan springs ("Fu" and "Ma",
133   Fig.1), which are representatives of the Fuliya brine type (see section 2.2) and the
134   Tiberias hot springs ("Ti", Fig.1). The profile runs through the Jordan Rift Valley,
135   which is at that location occupied by the lake. At mid-point between the western
136   and eastern shores, the profile turns to SE and crosses the Ha'on well ("Ha", Fig. 1),
137   the Lower Yarmouk Gorge ("LYG", Fig. 1) and ends in the Cretaceous limestone
138   outcrops of the Jordanian Ajlun Plateau. At its eastern part, the profile is nearly

139 perpendicular to both the geological structure and equipotential lines of the Ajlun
140 Cretaceous aquifer (El Nasser, 1991; BGR, 2001).
141   Along the studied profile, the groundwater levels vary from -150 m mean sea
142 level (MSL) in the Lower Galilee to -209 m MSL close the lakeshore (Water authority
143 of Israel, 2012). The regional water table in the Ajlun Heights reaches elevation of
144 50 m MSL at the end of the profile (BGR-WAJ, 2001). In the LYG, the observed wells
145 are artesian (Siebert et al., 2014).
146   The geological assumptions used to construct the profile shown in figure 2 are
147 based on Inbar (2012) and current interpretation of seismic data from the late 90's
148 (Ben Gay et al., 1997), as recalled here. The Golan Heights and the Ajlun are
149 separated by the LYG (Fig. 2) and are usually described as a continuous ENE-WSW
150 syncline (Meiler, 2011; Roded et al., 2013). According to Shulman et al. (2004), an
151 ancient fault at the LYG explains the huge difference of Jurassic thickness between
152 Ajlun and the Golan Heights, as reflected in the representative cross-section (Fig.2).
153   The ~3 km thick successions of the Triassic (Benjamini et al., 2005) and ~2 km
154 Jurassic sequences in the Lower Galilee (Hirsch, 2005) differ significantly from the
155 much thinner equivalent units in the Ajlun (400 – 500 m each). The Jurassic section
156 east of the Jordan Rift Valley is primarily composed of limestones and marls,
157 whereas the Jurassic in the west also hosts volcanics and dolomite. For that reason,
158 only one unit represents the Jurassic at east, whereas in the west it is subdivided
159 into four "sub-units" (Fig. 2).
160   Above, the Lower Cretaceous Kurnub Group of the Galilee comprises the Tayasir
161 Basalt and the continental sandstone of the Hatira formation (Table 2), attaining a
162 total thickness of nearly 400 m (Rosenfeld and Hirsch 2005). Opposite, in the Ajlun
163 area, the 200 m sequence of mostly coarse-grained Kurnub sandstone indicates a
164 fluvial deposition system with brief marine ingression (Abu Saad and Al Bashish,
165 1996) (Table 2). Accordingly, the different sediment fills significantly vary the
166 physical properties distribution, particularly the hydraulic conductivity (Table 2 and
167 section 3.2).
168   In both regions, intercalations of limestones and marls are building most of the
169 Upper Cretaceous sequence. In the Galilee, the Cenomanian-Turonian sequence is
170 composed mostly of well-bedded dolomites and limestones and while the Turonian
171 and Lower Senonian in the Ajlun is solely composed of limestone (Rosenfeld and
172 Hirsch, 2005; Makhlouf et al., 1996). The Senonian chalks and marls and the Eocene
173 limestones were deposited on a folded terrain, yielding thickness increases in
174 relative position to the synclinal axis (Flexer, 1964).
175   Zemah-1 borehole, located a few kilometers south of the lake ("Z" in Fig. 1),
176 reveals an outstanding thick succession of solid salt interbedded by limestones,
177 clastics and magmatic intrusions (Marcus and Slager, 1985). This unique assemblage
178 of units is named "Zemah Complex" (Inbar, 2012). Following the model suggested
179 by Inbar (2012) and current reinterpretation of seismic data close to the path of the
180 presented geological profile (Fig. 2), it seems that a salt dome is ascending along the
181 western fault of the Jordan Rift Valley. Therefore, it is assumed that below the lake
182 a salt body equivalent in time to the Zemah Complex is present (Fig. 2), the top and
183 depth of which are not known.

184

185

2.2. The anomalies: salinity and temperature

Total dissolved solids (TDS) and temperatures of spring and well waters (Table 1) are strongly dependent on the seasons. TDS is highly variable, ranging from almost freshwater conditions in the LYG to highly saline outflows in the Tiberias basin. If one compares temperatures and salinity (Fig. 3), three groundwater types can be distinguished: (1) brines from deep wells, (2) springs along the coastline of the lake and (3) fresh to brackish waters in the LYG. It can be seen that within the LYG, groundwater is heated up at great depths, and the low TDS indicates that mixing with deep brines plays a minor role (Siebert et al., 2014).

Ten meter below the lake bottom, time domain electromagnetic investigations indicate that salinity distribution is not homogeneous (Hurwitz et al., 1999), varying between 11 gL^{-1} and 22 gL^{-1}. Relatively fresh groundwater is detected beneath most of the shoreline because of freshwater advection from regional aquifers along the margins.

Overall, very scarce data on TDS is available at depths greater than -800 m MSL. According to the conceptual models of Abbo et al. (2003) the Cretaceous aquifers carry saline waters with chlorinity of 15 to 18 gL^{-1} (up to 48 gL^{-1} TDS), whereas the Eocene aquifers bear fresh water characterized by chlorinity between 0.03 and 0.3 gL^{-1} (up to 3.5 gL^{-1} TDS). This finding is in good agreement with the chlorinity-depth profiles by Greitzer (1980). Those profiles further show salinities in deeper units up to 120 gL^{-1} (172 gL^{-1} TDS in the Jurassic). Based on Br/Cl and Na/Cl molar ratios, the back-calculated TDS of deep brine yield to values of more than 300 gL^{-1} (Möller et al., 2012).

Groundwater temperatures vary strongly within the same cluster of springs (Table 1). Particularly, in the LYG (Mukhebeh and Hammat Gadder, "Mu and "HG" Fig. 1), the temperature difference between springs and wells that are less than 50 m apart can be more than 10 °C. Temperature vs depth profiles at Kinneret 10b ("K10b", Fig. 1) and Mezar ("M" in the LYG, Fig. 1) are shown in figure 4. The K10b well displays an inversion in the temperature trend at about -850 m (MSL). In geothermal systems, this type of anomaly is often associated with cool water flowing through fractures in the surrounding units. Such changes of temperature, however, can also be due to the drilling process or active pumping in the wells.

In general, while geothermal surveys indicate that the average conductive heat flux in Israel is rather low, around 40 - 45 mWm^{-2} (e.g. Eckstein and Simmons, 1997; Shalev et al, 2013), the area of the Lake Tiberias is overall affected by heat flow higher than 60 mWm^{-2}, locally reaching 85 mWm^{-2} (Shalev et al., 2008). Particularly, in the southeastern part of the study area, the temperature gradient inferred from deep wells in the LYG is 46 °C km^{-1} (Fig. 4) which is almost twice the average geothermal gradient of the area.

Two phenomena are attributed to this anomalously high gradient (Bajjali, 1994): (1) ascent of deep heated groundwater along fractures or (2) heat flow perturbations related to magmatic intrusions. Here, the impact of a fault on the heat transport processes in the LYG is numerically investigated.

The numerical models presented here are aimed to understand whether the observed anomalies are related to faults and hydrologic regimes, rather than quantifying the impact of local anthropogenic processes.

2.3. Geochemical evidences for brine movement

Numerous hydrochemical and isotope investigations have been carried out in the study area in order to understand the brine movements responsible for causing the hot saline springs. Mazor and Mero (1969), Gat et al. (1969), Hurwitz et al. (2000a, 2000b), Klein-BenDavid et al. (2004) and Möller et al. (2012) discuss various formations of brines. All studies agree that the observed saline waters are mixtures of meteoric water with some ascending relic brines.

Möller et al. (2012) suggests that these relic brine(s) are derivatives of evaporated seawater due to 1000Br/Cl molar ratios of 5.7, which resembles seawater evaporated by about 40% (McCaffrey et al., 1987). The observed relic brines result from the evaporation of seawater that remained trapped in the Rift sediments and adjacent sedimentary rocks during the last Mediterrean transgression. These relic seawater brines are henceforth referred to as source brines (SB).

Different mechanisms driving the SB in the basin have been suggested, as reviewed by Simon and Mero (1992). During its ascent, the SB mix with shallow circulating freshwater. The forces that are responsible for upward flow can be induced by compaction of sediments, tectonic stresses or density variations due to geothermal sources (Mero and Mandel 1963; Mazor and Mero, 1969). The latter often implies the generation of convective cells, as shown in numerical models of Gvirtzman et al. (1997a, 1997b). The topography-driven flow imposed by the surrounding heights (e.g. Eastern Galilee, Golan, Ajlun) provides an additional force that flushes deep-seated saline water toward discharge areas (Goldshmidt et al., 1967). Here, the topography-driven flow is also called "regional flow". The same process is referred to as forced convection in Gvirtzman et al. (1997a) or gravity-driven flow in Rimmer et al. (1999, 2003). Rimmer et al. (1999) and Abbo et al. (2003) considered variation of groundwater levels in aquifers showing that the springs discharge and salinity are sensitive to the near lakeshore boundary conditions. Kolodny et al. (1999), Moise et al (2000) and Möller et al. (2012; 2014) discuss leaching by recharge water of residual seawater evaporation brines from pockets.

While it is clear that faults play a major role in providing preferential pathways for fluid flow in the Eastern Galilee (Vengosh and Rosenthal, 1994), the presence of deep faulting in the LYG is still an open question. Beside the heat anomaly recorded there (sections 2.1 and 2.2), an additional indication pointing to active faults in the LYG is the high ^{3}He/^{4}He found in the sampled waters (Tsur, 2013; Kaudse, 2014). ^{3}He predominantly originates from the mantle and therefore implies that groundwater interacted with mantle fluids or volatiles rise though open fractures.

Depending on the interplay between the above described transport processes and the mixing ratio with the regional flow of freshwater, different types of brines form. Two main branches of brines are distinguishable:

(1) Brines along the eastern and southeastern shoreline of the lake and even south of the Yarmouk show low Na/Cl and high Br/Cl molar ratios resembling evaporated seawater. The most prominent brine is the Ha'on brine which best represents the diluted SB. A strongly diluted form of the SB appears in the springs of Hammat Gader ("HG", Fig. 1). Hammat Gader brines are essentially weathering solutions of the basaltic cover in the eastern catchment area. These spring waters

279 contain less than 3% of SB (Siebert et al, 2014). The waters nearby the Mezar deep
280 well ("M", Fig. 1) are recharged over limestones in the foot area of the Hermon
281 Massif (north of the Golan, out of Fig.2) and are very diluted too (Siebert et al.,
282 2014). The brines of Waqed ("W", Fig.1) and nearby Newe Ur wells are the most
283 southern ones that still show high Br/Cl and Mg>Ca but low Na/Cl ratios, typical of
284 evaporated seawater.

285   (2) Brines along the western shoreline of the lake, such as those of the Tiberias
286 hot springs, Fuliya and Tabgha clusters ("Ti,", "Fu", "Ta", Fig. 1), are interpreted as
287 derivatives of the SB (Möller et al. 2012; 2014) because they show similarly high
288 Br/Cl and low Na/Cl ratios like the SB.

289   Fuliya and Tabgha clusters ("Fu", "Ta", Fig. 1) are affected by Tiberias types of
290 water ("Ti", Fig. 1), which suggests northward movement of brines along the
291 syncline. The Golan topography imposes an additional flow of SB below the lake,
292 from east to west (Stiller, 2009).

293   The Na/Cl of SB at the western shore of the lake is slightly enhanced, but still
294 much below one, indicating local leaching of evaporites below the lake. Therefore,
295 it is highly unlikely that the salinity of the observed springs originate from leaching
296 of the Zemach salt plug (Möller et al., 2012).

297 **3.   Modeling Approach**
298 *3.1. Numerical model*

299   Transient simulations of coupled fluid flow, heat and mass transport processes
300 (i.e. thermohaline) are run in order to investigate the possible hydrological regimes
301 developing in the selected profile (Fig. 2**)**.

302   The commercial finite element (FE) software package FEFLOW (Diersch, 2002)
303 is used to solve the partial differential equations (PDE) of thermohaline flow. The
304 strongly coupled system of equations is given in the appendix A. FEFLOW® fully
305 implements variable-density and viscosity form of the Darcy law (Eq. A.1).
306 Polynomial fittings ensure that fluid density (Eq. A6) is dependent on the calculated
307 pressure, temperature and concentration. Only the liquid phase is considered and
308 fluid viscosity (Eq. A7) is pressure independent.

309   The simulations are run over 1 Myr. A semi-implicit time discretization scheme
310 with a maximum time step of 3 yr is used to advance the coupled equations. The
311 simulated time interval of 1 Myr does not represent a specific geological period but
312 allows the simulations to reach a quasi steady-state solution of the problem.

313   The two dimensional approach implies that all processes occur in the vertical x-
314 z plane, thereby neglecting convection parallel to the fault plane, which is the most
315 likely convective mode in fractured media (e.g. Simmons et al. 2008). Convection in
316 the fault plane determines the number of springs along the surface trace of the fault
317 (Lopez and Smith 1996), and further contributes to the migration of both heat and
318 brine. Additional cross-sectional flow cutting the profile is driven by the regional
319 topography that in turn controls the location of discharge areas. Furthermore, at
320 the turning point of the profile (Fig.1 and Fig.2) , it is not possible to apply any mass-
321 balance. While these aspects cannot be accounted in a two-dimensional approach,
322 the 2D patterns illustrated here are still useful indicators of the physical processes
323 and hydrogeological characteristics controlling the temperature and salinity trends

324 observed in the area. At the present state of the research, a 3D structural model of
325 the whole study area is built which will allow investigating the additional impacts of
326 cross-sectional flows and infer salinity mass-balance of the lake.

3.2. Structural setting and properties

328 The modeled cross section (Fig.2) consists of all units described in section 2.1,
329 except for the poorly constrained stratigraphy below the Triassic at the eastern end
330 of the profile. A basement at 6 km depth closes the model to apply heat flow
331 boundary conditions (Fig.5).
332 The physical properties of each unit (e.g. hydraulic conductivity, storage,
333 porosity and heat conductivity) are given in Table 2. The hydraulic values are mainly
334 adapted from previous numerical investigations (e.g. Gvirtzman et al., 1997a,
335 1997b; Abbo et al., 2003; Roded et al.,2013), conceptual models (e.g. Rimmer et al.,
336 1999) or pumping tests (eg. Bergelson et al., 1998). The model differentiates the
337 main aquifers and aquitards in the vertical direction (z). Furthermore, it also
338 accounts for heterogeneities along the x direction of the profile, as described in
339 section 2.1. By example, the presence of impervious basalt and clays at the base and
340 top of the northern Cretaceous is implemented by assigning a hydraulic conductivity
341 value lower than the one given at the southern side of the profile. The anisotropy
342 ratio of host rocks ($\frac{Kz}{Kx}$) is 0.015, in the range of values inferred by Hurwitz et al.
343 (2000a). By contrast, faults are isotropic, similarly to the investigations of Shalev et
344 al. (2007). Here, the hydraulic conductivity of the faults varies between 30 myr^{-1}
345 (Shalev et al., 2007) and 140 myr^{-1}. The thermal conductivity of the units is an
346 average estimated from the lithological descriptions given in Eckstein and Simmons
347 (1977) and Shalev et al. (2013). The molecular diffusivity value is equal to the
348 chloride self-diffusion coefficient used in the transient salt transport models from
349 Hurwitz et al. (2000b).

3.3. Fault model and mesh

351 Different well-established approaches exist to model fractures in porous media
352 (e.g. Blessent et al., 2014; Vujević et al., 2014). Here faults are modeled using the
353 Equivalent Porous Media approach (EPM), i.e. permeable units extending from the
354 basement to the top. This choice is dictated by the lack of structural inputs for fault
355 geometry that are required to apply other numerical approaches, such as discrete
356 features. Faults are 40 m wide, as in the EPM models of faults in the Dead Sea basin,
357 by Shalev et al. (2007). This fault aperture is very small compared to the kilometer-
358 scale of the flow movements studied here. This configuration is suitable for the EPM
359 approach as this study focuses on the migration of heat and contaminants over large
360 spatial and geological time scale rather than the local prediction of solute exchange
361 at the fault/unit interfaces. The numerical investigations of Abbo et al. (2003)
362 provide an additional example of EPM approach to model mass transport in the
363 faults of the Tiberias area.
364 The "Triangle" algorithm (Shewchuk, 1996) is used to build the finite element
365 mesh. The elements have variable width and preserve the stratigraphic geometries
366 (Fig. 5, zoom). Within the faults, the mesh resolution is approximately 10 meters,
367 i.e. at least four nodes discretize the fault aperture in the x direction. The mesh
368 allows to account for possible buoyant-driven flow within the faults. Element

369 spacing grows gradually from the fault flanks to 50 meters in the surrounding units
370 and basement. This spatial smoothing ensures that (Yang, 2006) : 1) the fault width
371 is in the same order of magnitude of the elements size at the interface, which
372 satisfies the EPM requirements and 2) diffusive-dispersive processes are correctly
373 simulated at the matrix/fault interface.

374 The whole profile comprises approximately 150,000 triangular elements
375 satisfying the Delaunay criterion. Finer meshes did not affect the calculated
376 patterns.

377 *3.4. Boundary conditions (BC) and initial conditions (IC)*
378 The set of equations describing the thermohaline problem (Appendix A) is
379 solved with respect to the primary variables hydraulic head (h), temperature (T) and
380 concentration (C). The boundary conditions are illustrated in figure 5.

381 - h: Based on the data provided in section 2.2, the head is set as follows:
382 At the top: a constant head (i.e. Dirichlet) is set along the eastern and western
383 sides of the lake. In the Lower Galilee, the regional water vary between -150 m
384 mean sea level (MSL) at the northern ending of the profile to -209 m MSL close
385 the lakeshore. The water table in southern ending of the profile is equal to 50
386 m MSL.
387 In the LYG, h is set slightly above the local topography in order to simulate
388 artesian conditions of the area.
389 Along the lakebed, a transfer boundary condition (i.e. Cauchy, Eq. (1)) accounts
390 for lake and groundwater interactions in the form a Darcy flux $\boldsymbol{q}(t)$ given by:
391 $$\boldsymbol{q}(t) = L\big(h_{ref} - h\big)\boldsymbol{n} \qquad \text{Eq. (1)}$$
392 where the reference head h_{ref} is -210 m MSL (average lake level) and the
393 coefficient of leakage L is 4e^{-2} yr^{-1} as estimated by Stiller et al., (1975). $\boldsymbol{n}$ is the
394 vector normal to the top surface of the profile**.**
395 No groundwater flow (i.e. Neumann) is allowed through the lateral boundaries
396 of the profile.
397 - T: At the top, a heat transfer (i.e. Cauchy) with a reference temperature
398 T_{ref} of 20°C is assigned. This open boundary condition (Eq. (2)) allows heat
399 outflow through the surface, governed by
400 $$\boldsymbol{q_T}(t) = \emptyset_T\big(T_{ref} - T\big)\boldsymbol{n} \qquad \text{Eq. (2)}$$
401 where the heat transfer coefficient $\emptyset_T$ = 0.13 WmK^{-1} corresponds to the heat
402 conductivity of the Quaternary sediments (Table 2) divided by the
403 representative element height (10 m). Accordingly, the calculated temperature
404 T can increase at the locations where thermal springs are predicted by the
405 model.
406 At the basement, previous simulations used variable heat fluxes ranging from
407 60 mWm^{-2} to 72 mWm^{-2} (Gvirtzman et al., 1997a) or 50 mWm^{-2} to 100 mWm^{-2}
408 (Roded et al., 2013) over different portions of the studied profiles, in order to
409 reflect the observed thermal anomalies of the area. Since the numerical
410 investigations presented here mainly focus on the impact of faults on
411 redistribution of heat and brine in the system, a constant heat flux is set along
412 the whole profile basement. Specifically, an undisturbed basal geothermal flux
413 (i.e. Cauchy) of 60 mWm^{-2} is set at the bottom of the model. This allows inferring
414 to which extent the observed temperature and salinity anomalies result from

415   hydrogeological features of the basin, such as circulation of thermal waters
416   through faults, rather than imposed deep crust anomalies.
417   Lateral boundaries of the cross-section are insulated (i.e. Neumann).
418   - C: A Cauchy mass transfer boundary condition (Eq. (3)) is set at the top,
419   analogously to the head and temperature boundary conditiona (Eq. (1) and Eq.
420   (2)). The mass flux $\boldsymbol{q_C}(t)$ is given by
421     $\boldsymbol{q_C}(t) = \emptyset_C\big(C_{ref} - C\big)\boldsymbol{n}$ **Eq. (3)**
422   The concentration reference C_{ref} is 0,22 gL^{-1} at the lake (average lake salinity)
423   and 0 gL^{-1} along the remaining portions of the top profile. The mass coefficient
424   transfer $\emptyset_C$ is 4e^{-2} yr^{-1}.
425   A constant concentration of 300 gL^{-1} is set at salt dome (UZC). FEFLOW® cannot
426   account for dissolution of salt and therefore the shape of the UZC does not
427   change with time.

428   The transient simulations are initiated as follows (Fig. 5):

429   - *h*: The initial conditions for hydraulic head are derived from steady state
430   simulations of groundwater flow.
431   - *T*: As for the hydraulic head, the initial temperature profile is purely conductive
432   (Fig. 5, top). Because of the high thermal conductivity of the UZC (Table 2),
433   isotherms are slightly bending at the salt edges. This phenomenon is very
434   common in geothermal basins hosting salt domes (e.g. O'Brien and Lerche,
435   1988).
436   -   *C*: In the paragraph 4.2, thermally-driven flow is coupled to brine
437   transport. For this purpose, based on the data and considerations described in
438   sections 2.2 and 2.3, an initial salinity condition is set to reflect the presence of
439   the relic source brines (SB) resulting from seawater evaporation , as illustrate in
440   figure 5 (bottom): the concentration increases from freshwater conditions
441   within the top aquifers (Eocene) to 250-300 gL^{-1} in the basement and UZC. This
442   assumption certainly does not reflect paleo-salinity conditions of the area nor
443   correctly represents the Plio-Miocene SB. Nevertheless, it allows studying the
444   impact of faults, heat and regional flow on the migration of the relic seawater
445   SB

446   **4.   Results and discussions**

447   Models of fluid transport processes over basin-scale and geological time periods
448 like those presented here cannot be calibrated and verified for temperature and
449 salinity at a given time and location. Nevertheless, the results are qualitatively fitted
450 to the temperature-depth profiles of the wells and the salinity ranges of the springs
451 described in section 2, by testing different fault permeability. This kind of "regional
452 calibration" allows investigating the major hydrogeological processes that control
453 the migration of heat and brine in the system.
454   *4.1. Scenario 1: Effects of geothermal flux on flow and temperature anomalies*

455   Following previous numerical studies of the area (e.g. Gvirtzman et al., 1997;
456 Roded et al., 2013), only equations A.1 to A.3 are solved here, i.e., no brine transport
457 is computed. Accordingly, fluid density and viscosity (Eq. A.6 and Eq. A.7) are not
458 dependent on the concentration C. This simplifying assumption is made to directly

459　compare the findings with those from previous studies and later infer the impact of
460　salinity (section 4.2).

461　　　Velocity and temperature fields resulting from the coupled fluid flow and heat
462　transport process are illustrated in figure 6 (top). In this scenario, all faults except
463　the minor one below the lake are permeable, with a hydraulic conductivity of 30
464　myr^{-1}, like in the simulations from Shalev et al. (2007). Two major independent flow
465　fields can be distinguished:

466　　　(1) A topography-driven flow (or regional flow) below the Lower Galilee and
467　southeastern heights discharges groundwater through the Turonian/Cenomaniam
468　and Upper Eocene units, respectively. Therein, the velocity ranges between 0.4 myr^-
469　^{1} to 1 myr^{-1}. Springs exhibit peak velocities between 3 myr^{-1} and 5 myr^{-1} at the fault
470　traces that border the lake and in the discharge area of the LYG. A sensitivity analysis
471　showed that springs flow rate per meter width reaches 3600 m^3yr^{-1} when the
472　hydraulic conductivity of the elements at the top of the fault is 400 myr^{-1} (e.g. gravel-
473　sand). Assuming springs to discharge over a km-long shoreline, the inferred spring
474　fluxes are in the same order of magnitude of the monitored ones.

475　　　(2) Different deep-seated convective flows are separated from the upper
476　regional flow by the major aquitards. A squeezed cell develops in the Jurassic Nirim
477　("JN", Fig. 6) within the northern part of the profile. The calculated Rayleigh number
478　of the Jurassic Nirim is much smaller than the critical value of the onset of thermal
479　convection, calculated according to the theory of Nield (1968). However, in the
480　presence of permeable faults, it is known that convection occurs also in units with
481　subcritical Rayleigh properties (McKibbin, 1986). Channeled buoyant flow in the
482　faults induces groundwater in the surrounding units to flow either in a convective-
483　like mode or directly toward the faults, like in the overlying Jurassic Zohar ("JZ", Fig.
484　6). Darcy velocities of a centimeter per year characterize this cellular regime, which
485　is one to two orders of magnitude weaker than the upper regional flow. In contrast
486　to the fault-induced groundwater flow in the Jurassic units at the northern side,
487　thermal buoyant forces generate Rayleigh convective patterns in the LYG and Golan
488　Heights. Two cells circulate groundwater below the Senonian aquitard at a
489　maximum velocity of 0.1 myr^{-1}. This is due to the presence of more permeable and
490　thick cretaceous horizons at depths which Rayleigh number is higher than the
491　estimated $Ra^{critical}$. As a result, the heat flow destabilizes the fluid density: the
492　vertically elongated cell below the Golan forces groundwater to descend from the
493　Upper Turnonian units (-1 km depth MSL) to the Lower Jurassic (-3 km depth MSL),
494　while deep groundwater rises mostly through the LYG fault and partly through the
495　Ha'on fault, at velocities close to 2 myr^{-1}. In this respect, deep-reaching faults
496　provide the only hydraulic connection between the deep convective systems and
497　the shallower regional flow, allowing thermal water to ascend from depths of -3 km
498　MSL. Discharging springs result from the interaction of these two regimes
499　supporting the chemical data that spring waters are a mixture of deep thermal
500　water and shallow groundwater.

501　　　The regimes described above strongly affect the temperature distribution (Fig.
502　6, bottom). At the northern part of the profile, the thermal water ascending to the
503　surface along the fault flanking the lake generates an elongated heat plume. Hot
504　groundwater is drained from the Jurassic units and flows out of the system at
505　temperatures between 50 °C and 60 °C. The tip of the heat plume spreads also
506　laterally toward the northern side of the profile because of the presence of open

507 faults that partly capture the ascending flow (Fig. 6, zoom). Therefore, groundwater
508 temperature can either vary of several degrees over the lateral temperature
509 gradient or decrease with depth. A simulation in which buoyant forces are not
510 computed (i.e. $\rho^f = \rho_o^f$ in Eq.(A.2)) prevents any heat plume to ascend from depths,
511 but reveals a local regional flushing through faults (i.e. advection) of groundwater
512 from Upper Turonian/Eocene formations, allowing a maximum spring temperature
513 of 32 °C. Both calculated temperatures are in agreement with the monitored spring
514 temperatures (Table 1), suggesting that thermal buoyant flow in the faults and
515 advection by regional flow are both possible heat transport mechanisms.
516 Below the LYG, the two convective cells generate an upwelling of deep
517 groundwater into the LYG fault, and a downwelling of colder water in the fault
518 below the Golan. Spring temperature in the discharge area of the LYG is 35 °C owing
519 to the presence of a strong regional flow in the upper Eocene unit that cools down
520 the rising thermal plume. The small upwelling observed at Ha'on is due to the local
521 groundwater outflow from the neighboring Golan, as also indicated by a spring
522 temperature of 30 °C.
523 The temperature-depth profiles along two boreholes, as located in Fig.6, show
524 a good fit with available well data (Fig. 7, red crosses and circles). The temperature
525 inversion observed at K10b well (red circles) is due to the spreading of the heat
526 plume toward neighboring permeable faults, as previously explained (Fig. 6, zoom).
527 If the fault at the western side of the K10b well is impervious, the heat plume cannot
528 spread laterally, leading to a linear vertical temperature gradient (Fig. 7, yellow
529 circles).
530 In the LYG (Fig. 7, red crosses), the presence of the fault allows the temperature
531 gradient to be steep even under normal basal heat flow conditions. Interestingly,
532 without the LYG fault, the convective plume persists and the temperature trend is
533 preserved (Fig. 7, yellow crosses). However, since hot water is not anymore
534 channeled upward, the calculated temperatures are lower compared to the case
535 with fault (Fig. 7, red crosses).
536 Gvirtzman et al. (1997) models display similar patterns below the Golan. The
537 simulations of Roded et al. (2013) display a thermal plume discharging upward in
538 the LYG. However, those results are inferred from simulations that do not account
539 for salinity effects, as discussed in the next section.

540 *4.2 Scenario 2: coupling with salinity*

541 Here the fully coupled system of flow, heat and mass (i.e. salt) transport
542 processes is solved (Eq. A.1 to A.7). The EOS account for pressure, temperature and
543 salinity effects. It is worth recalling that an initial salinity distribution is set to model
544 the SB that originally saturates the units. It is assumed that the TDS of the SB
545 increases from freshwater conditions at ground level, to 300 gL^{-1} at the salt dome
546 (Fig. 5 bottom, and section 3.4).
547 When the hydraulic conductivity of the faults is 30 myr^{-1} (as in the purely
548 thermal simulations, paragraph 4.1), this initial salinity distribution overwhelms the
549 convective regimes in the deep units and prevents any thermal buoyant flow in the
550 faults (i.e. no thermal plume) that was previously observed in the scenario without
551 salinity (section 4.1). Salinity also increases the dynamic viscosity of the brine (Eq.
552 A.7) and therefore reduces the effective hydraulic conductivity of the sediments (Eq.

553 A.5). As a result, the only observable process is the topography-induced flow that
554 flushes SB at the lake shores and through the LYG.
555   A sensitivity analysis reveals that by increasing the hydraulic conductivity of the
556 faults to values ranging between 90 myr^{-1} to 140 myr^{-1} triggers buoyant flow and
557 best fits the measured temperature data (Fig. 7, green crosses and circles). The
558 results of this scenario are illustrated in figure 8 and can be compared with figure 6
559 (no salinity scenario, section 4.1). The western fault flanking of the Jordan Rift Valley
560 and the LYG fault remain the preferential pathways for upward flow of thermal
561 water. While the flow patterns of the topography-driven flow in the upper units is
562 qualitatively similar to the previous case (section 4.1- point 1), the deep convective
563 regimes (section 4.1- point 2) are different. The cell below the Galilee Mountains
564 develops into the Upper Jurassic Zohar ("JZ", Fig. 8), creating a wide stagnant zone
565 below it (Fig. 8). Hence, thermal waters that ascends along the western fault of the
566 Jordan Rift Valley originate at depths between -2 km MSL. Also at the southern side
567 of the profile, the cellular patterns are different from those calculated in a purely
568 thermal regime (compare Fig. 8, top and Fig. 6, top). The flow below the Ajlun is not
569 anymore convective but directed toward the LYG fault. Groundwater in the
570 overlying Turonian unit is not fully drained by the Ha'on fault and can flow westward
571 below the lake into the discharging fault. Darcy velocities characterizing this
572 movement into the sedimentary fill are however very slow, at maximum 1 cmyr^{-1}.
573 Geochemical evidences, as explained in section 2.3 (point 2), also request this brine
574 movement. In its lower part, the cell stretches toward the salt flank where
575 downward flow is dominant.
576   Salinity and temperature distributions resulting from these hydrologic regimes
577 are illustrated in figure 8 (bottom). The evolution of the SB can be inferred by
578 comparing Fig. 5 (bottom) and Fig. 8 (bottom). The steep syncline structure of the
579 units in the Lower Galilee enhances gravity-driven flow, which flushes the relic
580 brines. Overall, wide areas of diluted SB bearing less than 0.1 gL^{-1} TDS characterize
581 the Upper Cretaceous units in direct relation to the topography-driven flow below
582 the major Heights. Salinities are 2.5, 6 and 1.5 gL^{-1} at the western shore spring,
583 Ha'On well and LYG springs, respectively. The concentration profile exhibits areas of
584 diluted brine at the eastern shoreline, because of the inflow of freshwater from the
585 surrounding regional flow, as observed by Hurwitz et al. (1999). Accordingly, by
586 decreasing the hydraulic conductivity of the cover basalt, the salinity near Ha'on
587 increases to the monitored values (Table 1.).
588   Brine migration is strongly coupled with the heat transport in the faults. As
589 explained in the previous section, neighboring open faults can capture ascending
590 thermal waters (Fig. 6, zoom). As a result, the brine plume at the northwest side of
591 the lake spreads 2 km inland over the lateral temperature gradient (Fig. 8, zoom).
592 Therein salty groundwater is a mixture of relic seawater (SB) flushed by the
593 freshwater regional flow through the northern Turonian units and buoyant thermal
594 brines that reach the surface through the faults. Those brines likely contain
595 additional fingerprints of dissolved evaporites lifted up either through the fault
596 adjacent to the diapir crest or transported by the S-N flow above it (Fig. 8, top). By
597 contrast, on the opposite side of the diapir flank, gravity-driven flow constrains
598 heavy brine into the deep Jurassic/Triassic units. The thermal plume in the LYG has
599 the potential to drive relic SB from Turonian/Senonian units toward the gorge. This
600 upward flow is further enhanced by the regional flow from the Ajlun. As a result,

601 the plume is narrow (i.e. diluted) and the isotherms at the southern side of the
602 profile are flat compared to those resulting from the purely thermal regime (Fig. 6).
603 Contrarily to the previous scenario, without the LYG fault no thermal plume
604 develops: heavy brines endure a lateral/downward migration at depths and the
605 isotherms are close to the conductive regime.

606   *Impact of salt diapir and faulted lakebed*

607   A simulation initiated with freshwater conditions (i.e. 0 gL^{-1} everywhere except
608 the salt dome) is run in order to infer the impact of brine diffusion from the salt
609 diapir. The results show that no brine reaches the surface. Only a light salty plume
610 above the salt crest diffuses below the western shore of the lake with maximum TDS
611 of 0.2 gL^{-1}, which supports the hydrochemical evidence of leached evaporites in the
612 wells along the western side of the lake (Möller et al., 2012) and not in Ha'On well.
613 The presence of a permeable fault crossing the lakebed does not strongly affect the
614 large-scale patterns of heat and salt transport within the profile. Only a local effect
615 on the salinity distribution below the lake is observed. The calculated concentration
616 of the offshore spring is 6.7 gL^{-1}, and its temperature is 22 °C. Because of the
617 westward flow in the sedimentary fill, additional SB and salty water diffusing form
618 the salt crest can reach onshore springs. Consequently, the calculated concentration
619 of the western spring increases to 3 gL^{-1}.

620   The 2D limitation of these models prevents the assessment of additional brine
621 and heat flow from cross-cutting faults, such as from Tiberias to Fuliya, and
622 transversal regional flow. Also, the models do not account for overpressured
623 aquifers that can further increase upward heat and brine migration. These two
624 aspects could explain the extremely high salinity of the Tiberias springs (Table 1),
625 which cannot be reproduced by the simulations.

626   5. Summary and conclusions

627   Available hydrochemical data indicate that the thermal springs in the Tiberias
628 Basin (TB) mainly discharge deep waters that represent diluted source brines (SB),
629 resulting from evaporation of seawater of the last Mediterranean transgressions.
630 Geothermal data and geological considerations on the TB suggest that fault-
631 controlled hydrothermal processes generate the anomalous temperature
632 inversions observed at depths and the upsurge of hot/saline spring waters. The
633 variable salinity of the springs is due to the changing rates of the freshwater
634 topography-driven flow (regional flow).

635   First, numerical simulations of coupled heat and flow processes (without salinity
636 effects) are run over a representative geological profile of the area to gain insights
637 into heat transport in the system (section 4.1, Fig.6). The hydrothermal behavior of
638 the system is the expression of two different large-scale flow patterns separated by
639 the Cretaceous aquitards (Table 1). (i) A topography-driven flow rapidly discharges
640 groundwater at lowlands. In this regional movement, groundwater gains heat while
641 flowing through the Turonian and Eocene units. The springs temperature is around
642 30°C. (ii) The underlying convective regimes are either induced by ascending hot
643 waters in the faults or by density instabilities in the thick permeable Cretaceous
644 units below the LYG. Both types of cells are observable under an undisturbed basal
645 heat flow regime of 60 mWm^2, which is a representative value for the study area.
646 Buoyant flow of thermal waters in the faults can explain temperature higher than
647 30 °C observed at some springs. In this regard, the results are in good agreement

648 with available data (Fig. 7, red). Temperature inconsistencies recorded at the same
649 depth of different wells may reflect the diverse hydrogeological behavior of the
650 surrounding faults. Besides permitting upsurge of hot water, permeable faults
651 induce radial temperature gradients by partly capturing upward groundwater flow
652 (e.g. K10b well), or by allowing recirculation of cool groundwater from shallower
653 units, as in the fault below the Golan Heights (Fig. 6, zoom). It turns out that in a
654 freshwater environment the thermal plumes in the LYG form even without a fault.
655 This is due to the convective downwelling of cool water in the Golan Heights that
656 pushes hot water toward the LYG.

657 In the thermohaline simulations (section 4.2), an initial salinity representing
658 evaporated seawater brine, the source brine (SB), is implemented (Fig. 5, bottom).
659 It turns out that only the regional flushing in the shallow units is observable and the
660 deep heat transport is close to conduction, overwhelmed by the initial salinity
661 distribution. Topography-driven flow alone cannot support the anomalous
662 temperature profiles observed in the wells nor springs temperature above 30°C. The
663 anomalies are numerically reproduced by further increasing the permeability of the
664 faults (Fig. 7, green and Fig.8, zoom). Besides transporting heat, permeable faults
665 permit the regional flow to dilute and flush the SB. In this regard, the hydraulic
666 conductivity of the Quaternary sediments and the basalt cover also plays an
667 important role on the discharge rates of the springs. The springs of Hammat Gadder
668 in the LYG discharge highly diluted SB. By contrast, at depth below -2. 5 km MSL,
669 areas of highly saline and quasi-stagnant SB, as well as downward gravitational flow
670 from the salt body, characterize the whole profile.

671 Northwestward groundwater flow may have the potential to transport small
672 amount of salt from shallow salt bodies below the lake. Instead, no brine plume
673 from salt diapir reaches Ha'on, at the eastern side of the lake.

674 To some extent, the presented results are illustrative of the present day
675 situation because of the lack of paleo data and the static nature of the structural
676 features of the model. Nevertheless, the results provide the basis to extend the
677 models to a three dimensional scenario. 3D models of selected areas of the TB are
678 currently being build and will allow studying the different convective modes in the
679 fault planes, that can explain the complex brine movements along the master faults.

680 **Acknowledgments**

686
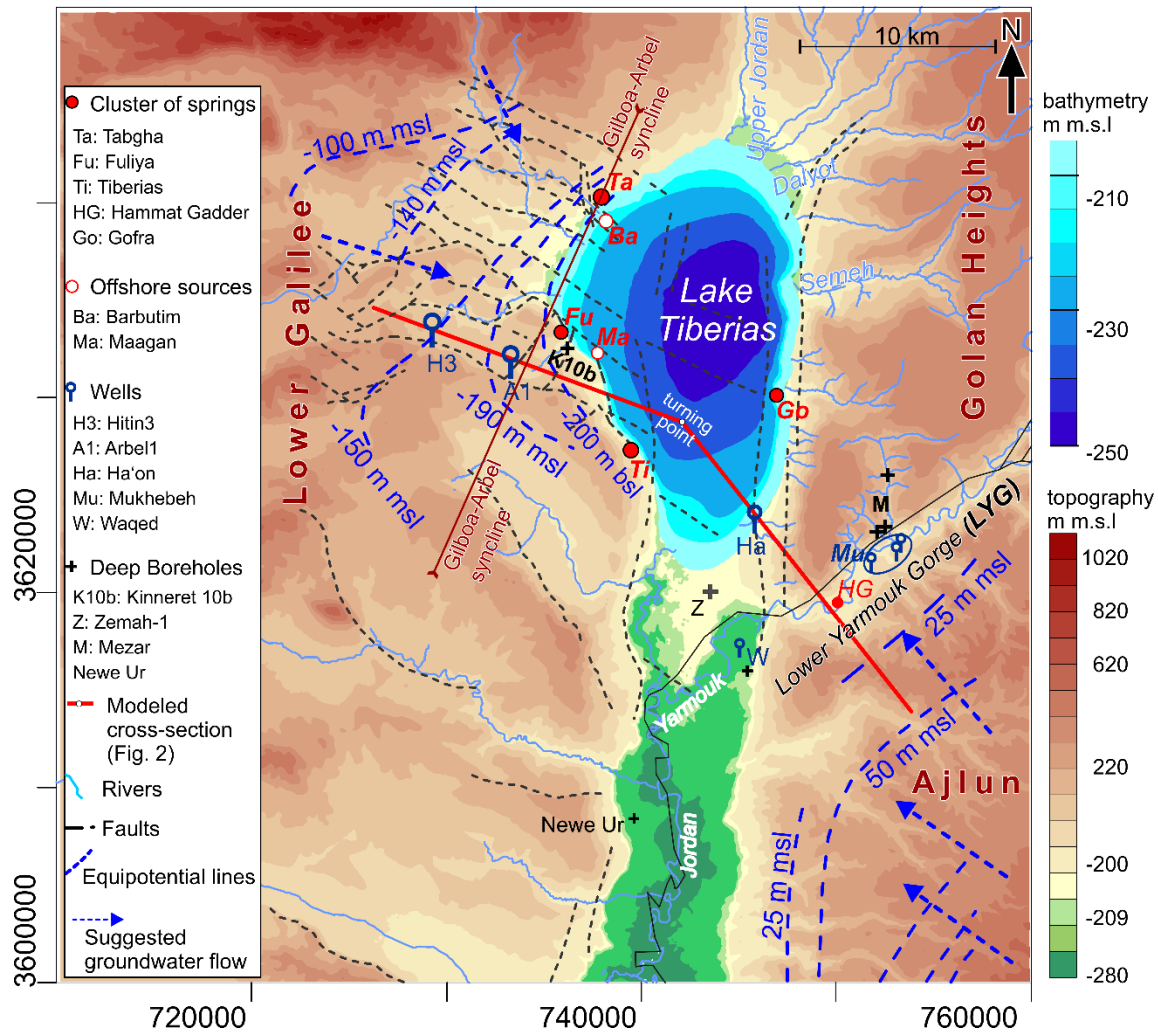
Fig. 1.The Tiberias Basin (TB). Study area including: location of the modeled cross section (Fig. 2), topography and lake bathymetry (SRTM data, Reuters et al. 2007), major faults (Ben-Avraham et al., 1996; Hurwitz et al.l, 2002c; Reznikov et al., 2004), clusters of springs, wells, deep boreholes, equipotential lines mean sea level (Water Authority of Israel, 2012; BGR 2001) and suggested groundwater flow directions (Bergerlson et al. 1998). **LYG**: Lower Yamourk Gorge.

Location "Cs": cluster of springs, "w" : well, "b": borehole	Abbreviation	TDS (g L^{-1}) range	Temperature (°C) range
Tabgha (Cs)	Ta	2.25 – 5.23 [1]	19 – 29 [1]
Fuliya (Cs)	Fu	2.06 – 2.72 [1,7]	27 – 30 [4,7]
Tiberias Hot Spring	Ti	28.94 [1]	64 [4]
Mukhebeh (Cs)	Mu	0.5 [9]	33 – 43 [9]
Hammat Gader (Cs)	HG	0.64 – 1.22 [1,9]	28 - 50 [1,7]
Gofra (Cs)	Go	5.07 [7]	32 [7]
Hitin 3 (w)	H3	0.48 – 0.517 [6,7]	25.8 [7]
Kinneret 10 (b)	K10b	24.7 – 31.7 [,7]	46 – 52 [7]
Ha'on (w)	Ha	14 – 22.5 [1,7]	24 – 35 [1,7]
Zemah-1 (b)	Z	220	-

Table 1 Range of temperatures, Total Dissolved Solids (TDS) and flow rates for the major cluster of springs (Cs), wells (w) and boreholes (b) as located in figure 1. The values are adapted from selected publications (superscript number) and do not provide a strict minimum-maximum interval.

1 - Möller et al. (2012), 2 - Abbo et al. (2003), 3 - Water Authority of Israel (2012), 4 - Gvirtzman et al. (1997a, 1997b), 5 - Rimmer (2003), 6 - Bergelson et al. (1998), 7 - Bergelson et al. (1999), 8 - Levitte and Eckstein (1978), 9 – Baijjali et al. (1997)
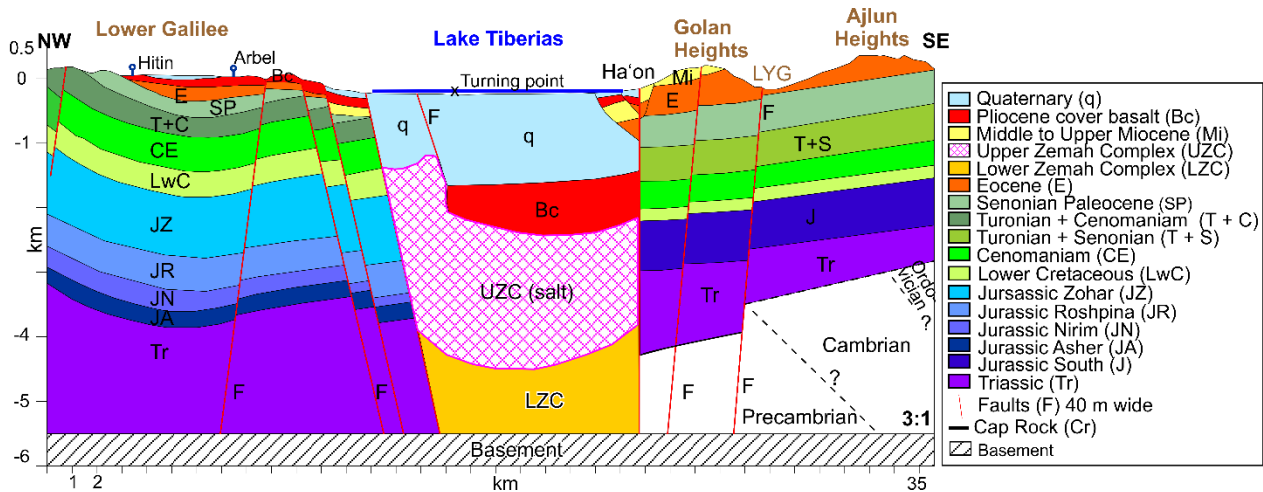
Fig. 2. Representative NW-SE cross section from Upper Galilee (Israel) to the Ajlun (Jordan) including wells and Lower Yarmouk Gorge (LYG) locations. Vertical exaggeration 3:1. Based on Saltzman et al. (1964), BGR (1993), Inbar (2012), Meiler (2011). In the southern ending of the profile, question mark symbols (?) refer to geological features that remain poorly constrained and are not implemented in the numerical model. The presence of a fault in the LYG is still debated. The physical properties of the different units and their values are listed in Table 2.

Epoch		Unit abbreviation	Segment of the profile (NW - SE)	Formation	Lithology	kx,y (m/yr)	storage 10^{-6} (1/m)	Poro (I)	Heat cond (W/m/K)
Quaternary	Holocene Pleistocene	Q		Dead Sea Gr.	Dead sea silt, marl, mudstone, sandstone	0.5	2.0	0.2	1.3
Tertiary	Pliocene	Bc		Cover basalt	mostly basalt, sediments	2 - 10	1.0	0.05	1.7
	Miocene	UZC		Upper Zemah Complex	mostly salt	imp.	0.2	0.01	3.6
		LZC		Lower Zemah Complex	mostly gabro & carbonate	0.010	0.2	0.01	2.1
		M		Hordos Fm.	conglomerates	5.0	1.6	0.08	2.1
	Eocene	E		Avedat Gr.	limstones	10.0	1.0	0.05	2.1
	Senonian	SP	NW	Mt. Scopus Gr.	chalk & marl - aquitard	0.5	2.0	0.1	1.5
		SP	SE	Muwaqqar Fm.	chalk & marl - aquitard	1.0	1.6		1.5
Upper Cretaceous	Upper Cenomanian - Turonian	T+C	NW	Bina & Sakhnin Fm.	limestone	200.0	3.0	0.15	2.1
	Turonian - Senonian	T+S	SE	B2-A7 (Wadi es Sir, Wadi um Ghudran, Amman silicified limestone, Al Hasa Fms.)	mainly limestone - Aquifer	73.0	2	0.1	2.1
	Cenomanian	CE	NW	Dier Hanna	limestone, dolomite interbedded with marls - aquitard	50	2.0	0.1	2.3
				Kamon	dolomite (some marls) - aquifer				
				Shueib	marly limestone - Aquitard				
		CE	SE	Hummar	dolomitic limestone- Aquifer	36.5	3.0	0.15	2.5
				Fuheis	marl - Aquitard				
				Na'ur	marly limestone - Aquifer				
Lower Creataceous		LwC	NW	Kurnub Gr., Hatira, Taysar basalt	Basalt and sandstone	6	1.6	0.08	2.2
		LwC	SE	Nebi Said	mostly permeable sandstone	110	3.0	0.15	
Jurassic		JZ		Zohar, Haluza, Sderot	limestone and dolomite	10	1.0	0.05	2.8
		JR	NW	Rosh Pina	marl	0.1	0.6	0.03	2
		JN		Nirim	limestone and dolomite	10	1.0	0.05	2.8
		JA		Asher	basalt and pyroclastics	5	1.6	0.08	2.2

	J	SE	Azab	primarily composed of limstones, interbedded with marls	22	0.8	0.04	2.5
Triassic	Tr				0.01	0.2	0.01	2.7
Permian	Basement	Zenifim	Arkose	imp.	0.2	0.01	2.5
	F		Faults	equivalent porous media	29 - 140	4.0	0.2	1.1

Table 2 Units, stratigraphy and values of the physical parameters of the modeled units. The stratigraphy is based on Inbar (2012) and BGR –WAJ reports (1993). The assigned values are adapted from Gvirtzman et al. (1997a, 1997b), Bergelson et al. (1998), Shalev et al. (2007, 2013), Roded et al. (2013).
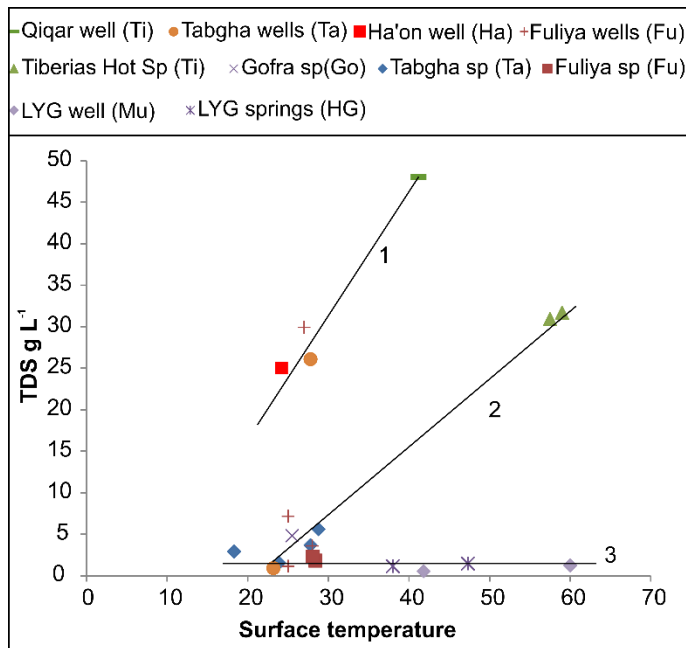
Fig. 3 TDS vs surface temperature correlations for deep wells (1), springs along the lakeshore (2), LYG springs and wells (data after Möller at al., 2014). For locations, refer to figure 1. Qiqar well belongs to the Tiberias cluster of springs.
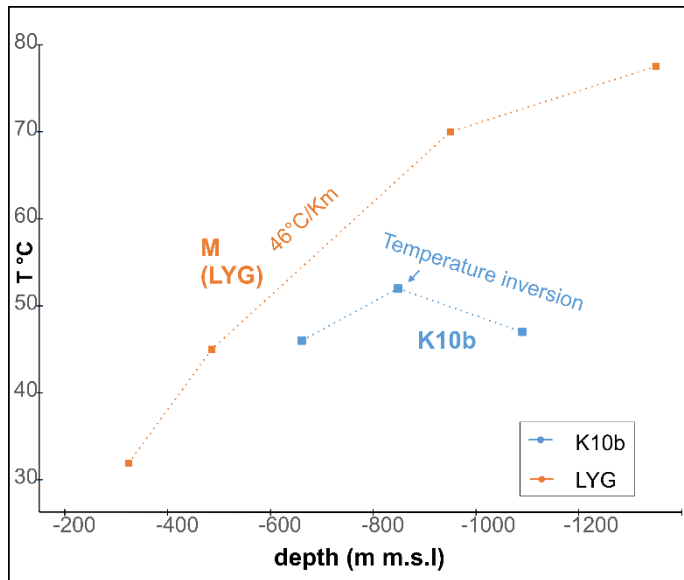
733
734 **Fig. 4**. Temperature profile in the Mezar (M) in the LYG (Roded et al. 2013) and in
735 the Kinnereth 10b (K10b) boreholes (Michelson et al., 1995). The studied profile
736 crosses the LYG at approximately -150 m msl, K10b wellhead is at -208 m m.s.l.
737 Linear interpolations (dashed lines) do not represent the actual temperature trends.
738 The geothermal gradient for the Kinnereth borehole is estimated by Gvirtzman et
739 al. (1997b).
740
741
742
743
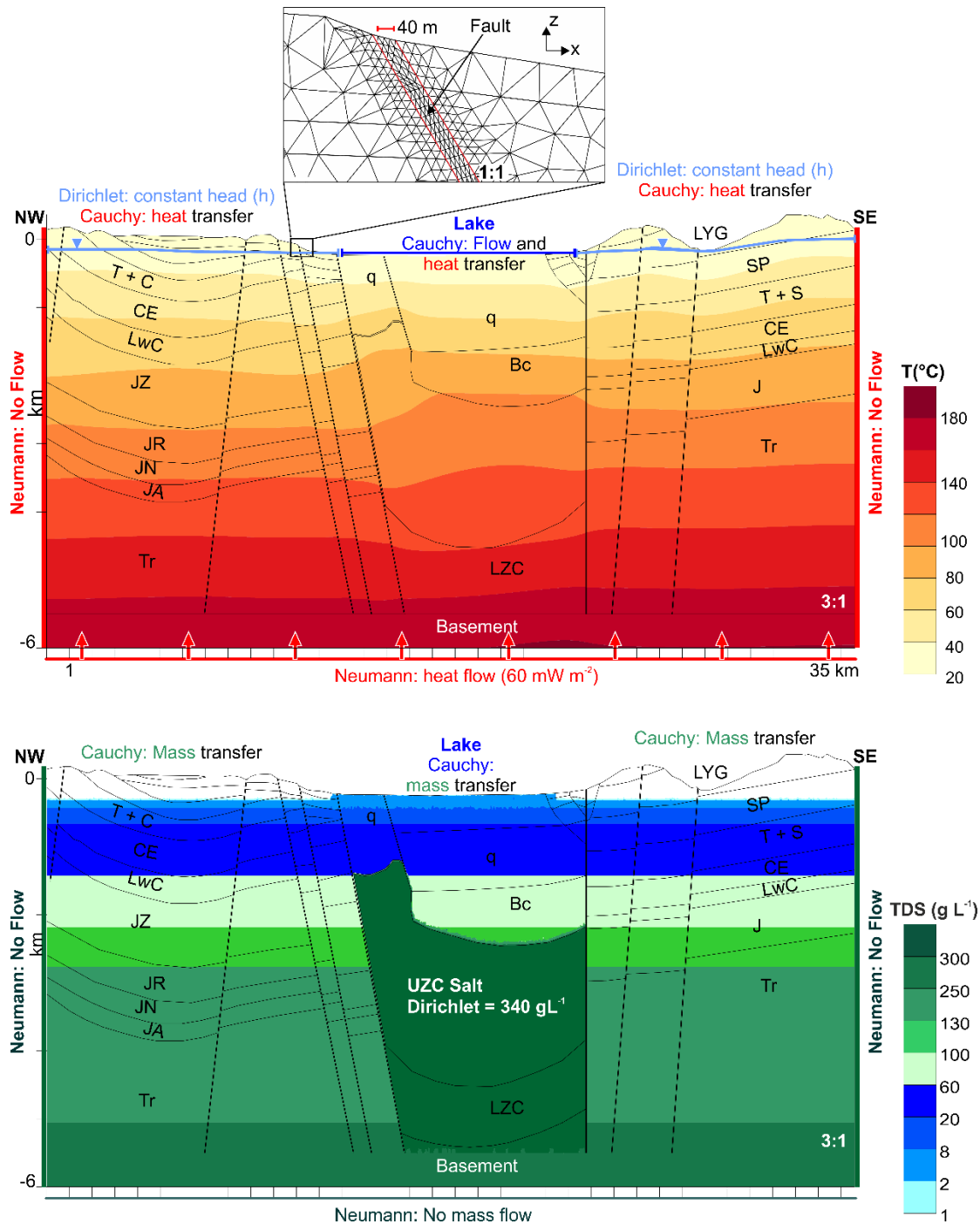
Fig. 5: Boundary and initial conditions. **Top:** Initial temperature (T) distribution (filled contours, in °C) with applied flow and temperature boundary conditions (blue and red lines). Vertical exaggeration 3:1. The local zoom (no vertical exaggeration) shows the triangular finite-element mesh in the fault (40 m wide) and surrounding units. Local refinements ensure that at least four elements discretize the whole fault in the X direction. **Bottom**: Initial TDS (C) distribution (filled contours, in gL^{-1}) with applied mass boundary conditions (green lines). This salinity profile initiates the transient thermohaline simulations described in paragraph 4.2. It represents an imaginary source brine (SB) resulting from relic evaporated seawater that saturates the units. Salinity constraints are based on the geochemical data given in paragraph 2.2. Vertical exaggeration 3:1. For units abbreviations, refer to figure 2 and Table 2

21
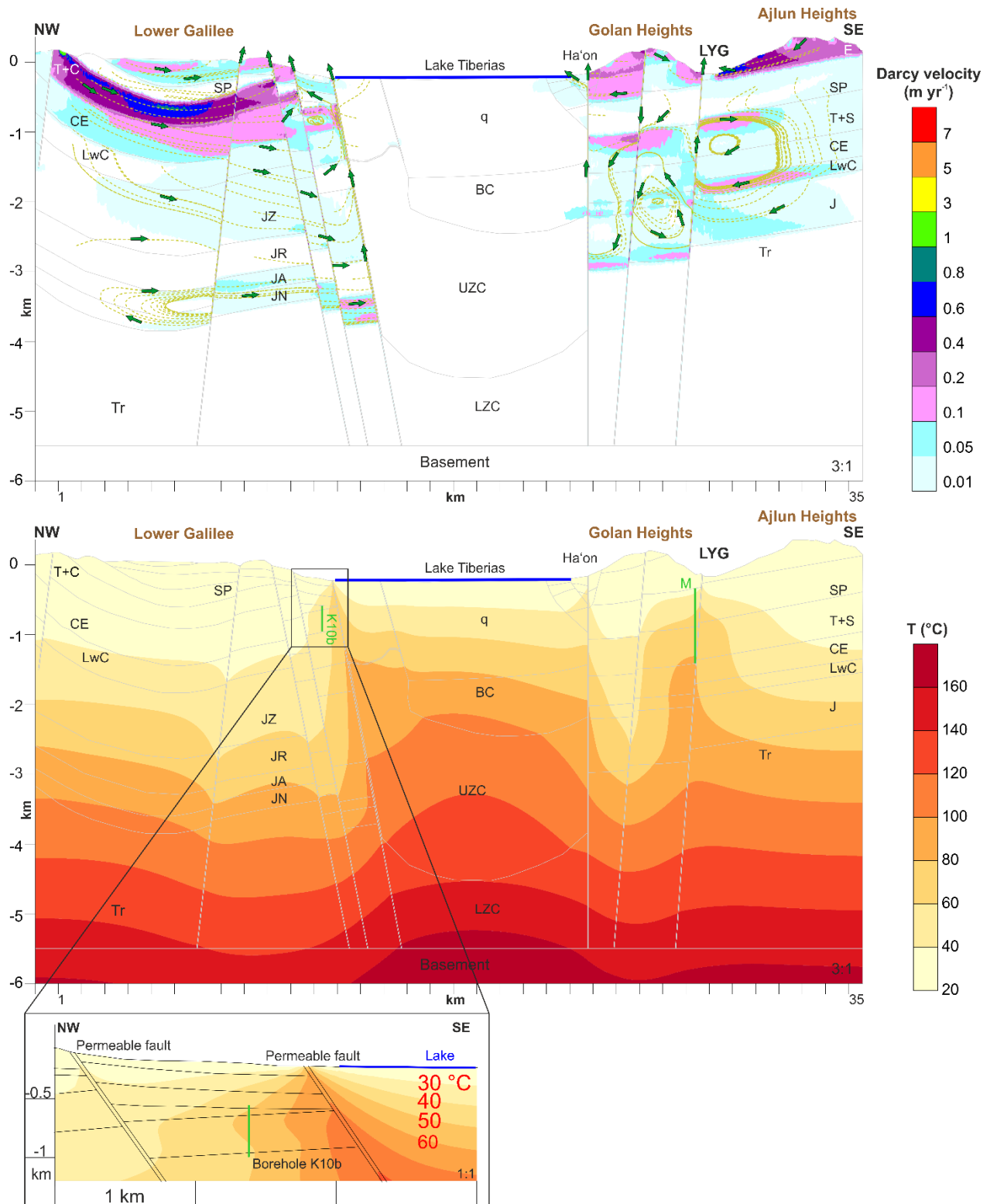
754
755 **Fig. 6:** Scenario 4.1 without salinity effects. **Top** – Colored patterns represent the velocity field (Darcy flow in
756 meter per year) and green dashed lines indicate flow paths (no streamline). Arrows show flow direction. No flow
757 lines are plotted in low velocity field (i.e. lower than 1 cm yr^{-1}). **Bottom** – Calculated temperature profile (°C).
758 Green vertical lines locate two boreholes based on the depths of the Kinnereth 10b (K10b) and Mezar (M, in the
759 LYG) deep wells. The temperature-depth profiles of these two boreholes are illustrated in Fig. 7. The zoom shows
760 the lateral spread of the heat plume due to the presence of a parallel permeable fault.
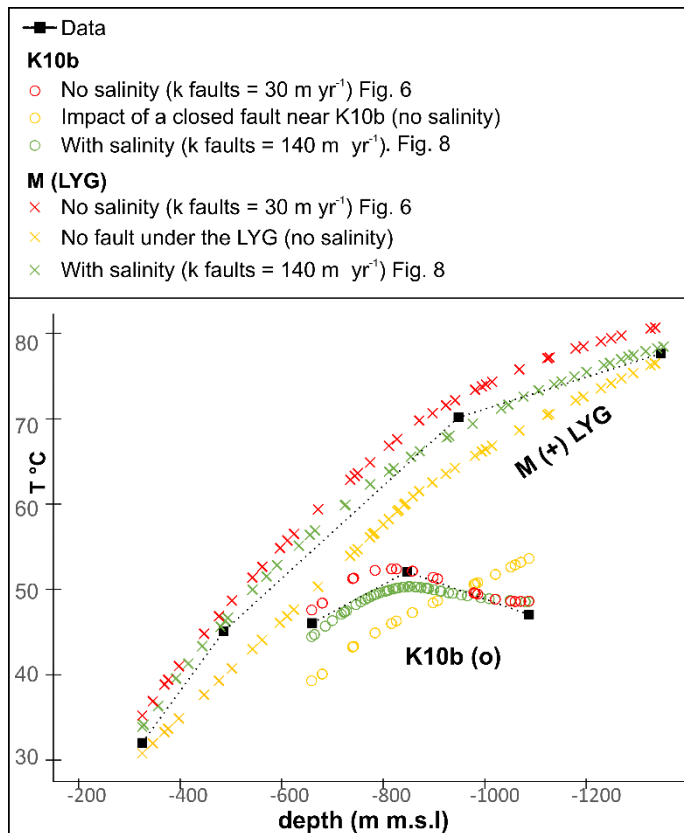
22

Fig. 7. Calculated temperature-depths at northern (K10b, circles) and southern (M, crosses) sides of the profile compared to field data (squares, Fig. 4). The boreholes are located in Fig.6, bottom and Fig. 8. These putative boreholes are just an illustrative example based on real depths, to show the different temperature trends. Red: scenario in which mass transport is not computed (i.e. no salinity effects, section 4.1). The hydraulic conductivity of the faults is 30 m yr^{-1}. Green: scenario with brine transport (section 4.2) is 140 m yr^{-1}. Yellow: impact of a closed fault near K10b and absence of the fault in the LYG, no buoyancy from salinity effects.
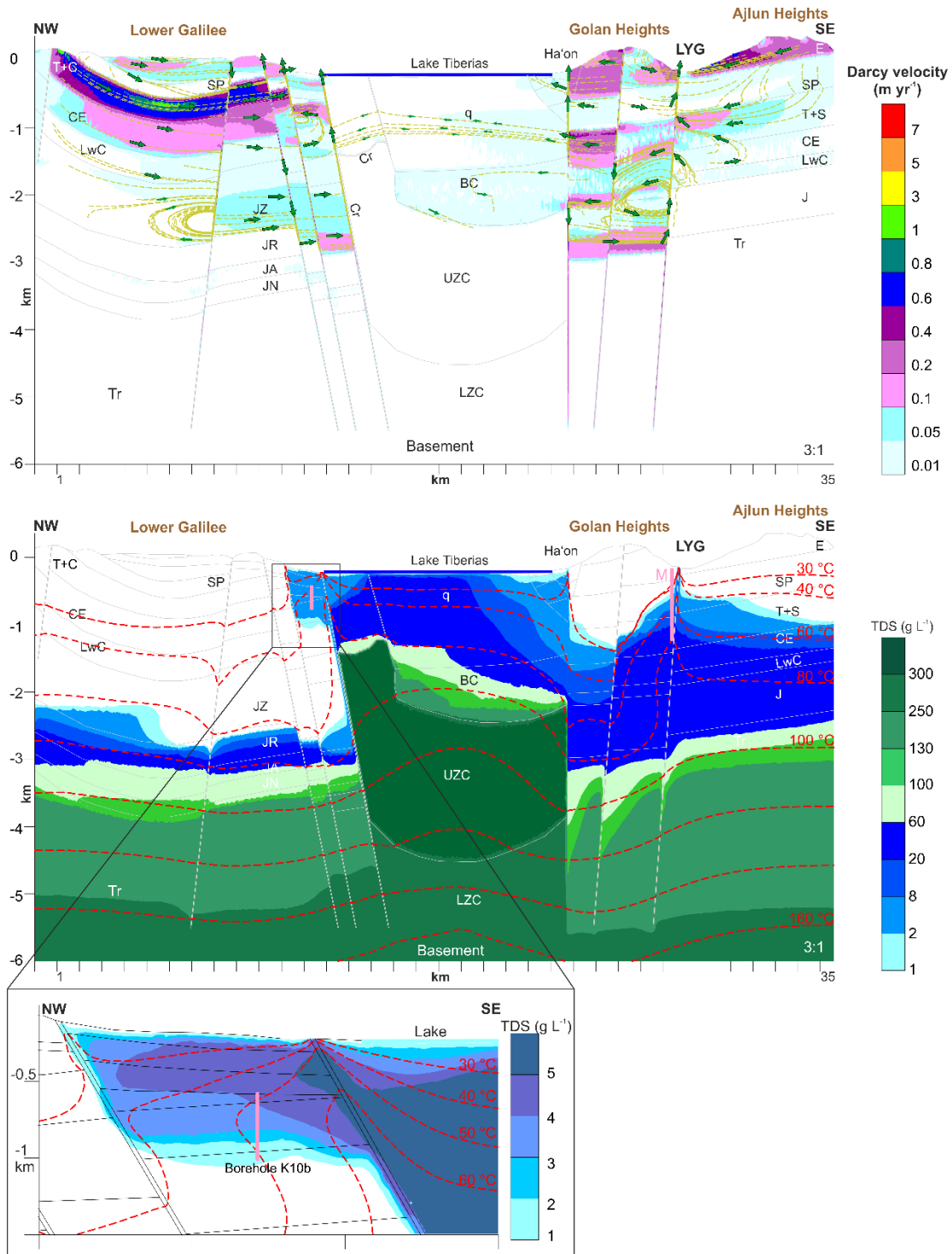
Fig. 8: Scenario 4.2 showing the effects of salinity. **Top** – Colored patterns represent the velocity field (Darcy flow in meter per year) and green dashed lines indicate flow paths (no streamline). Arrows show the flow direction. No flow lines are plotted in low velocity field (i.e. lower than 1 cm yr^{-1}). Small arrows in the sedimentary fill below the lake further highlight the very low velocity field. **Bottom** – Calculated TDS (gL^{-1}) of the source brine distribution and temperature profile (°C, red dashed lines). Heavy brine from the salt diapir (UZC) remains deep-seated, as explained in the section "Impact of salt diapir and faulted lakebed". Pink vertical lines locate two boreholes based on the depths of the Kinnereth 10b (K10b) and Mezar (M, in the LYG) deep wells. The temperature-depth profiles of the two boreholes are illustrated in Fig. 7. The zoom shows the lateral spread of the heat and brine plume due to the presence of a parallel permeable fault.

24

References

782   Abbo, H., Shavit, U., Markel, D., Rimmer, A., 2003. A numerical study on the influence
783   of fractured regions on lake/groundwater interaction; the Lake Kinneret (Sea of Galilee)
784   case. Journal of Hydrology, 283(1–4), 225-243.

785   Abu Saad, L., Al Bashish , M., 1996. Surface and subsurface lithostratigraphic
786   relationships of the Kurnub Sandstone Group in Jordan. Subsurface Geology, Bulletin 9, pp.
787   76.

788   Bajjali, W.T., 1994. Recharge and regional circulation of thermal groundwater in
789   northern Jordan using isotope geochemistry. Ph.D Thesis, University of Ottawa, Canada,
790   Ottawa, Canada, 211 pp.

791   Baijjali, W., Clark, I.D., Fritz, P., 1997. The artesian thermal groundwaters of northern
792   Jordan: insights into their recharge history and age. Journal of Hydrology, 192(1–4), 355-382.

793   Ben-Gay, Y., Reznikov, M., 1997. Multichannel seismic survey at the Sea of Galilee.
794   733/167/97, Geophysical Instittute of Israel.

795   Benjamini, C., Hirsch, F., Eshet, Y., 2005. The Triassic of Israel. In: J.K. Hall, V.A.K., F.
796   Hirsch, C. Benjamini, A. Flexer (Ed.), Geological Framework of the Levant Volume II: The
797   Levantine Basin and Israel. Historical Productions Hall, pp. 331-360.

798   Bergelson, G., Nativ, R., Bein, A., 1998. Assessment of Hydraulic Parameters of the
799   Aquifers Around the Sea of Galilee. Ground water, 36(3), 409-417.

800   Bergelson, G., Nativ, R., Bein, A., 1999. Salinization and dilution history of groundwater
801   discharging into Lake Tiberias, Israel. Applied Geochemistry, 14, 91-118.

802   BGR (Deutsche Bundesanstalt für Geowissenschaften und Rohstoffe), WAJ (Water
803   Authority of Jordan), 1993. Groundwater resources of Northern Jordan. Structural features
804   of the main hydrogeological units in Northern Jordan, vol 3. BGR-Archive No. 112708,
805   Amman, Jordan.

806   BGR (Deutsche Bundesanstalt für Geowissenschaften und Rohstoffe), WAJ (Water
807   Authority of Jordan), 2001. Groundwater Resources of Northern Jordan – Contributions to
808   the Hydrology of Northern Jordan, vol. 4. Ministry of Water and Irrigation, Amman, Jordan

809   Blessent, D., Jørgensen, P.R., Therrien, R., 2014. Comparing Discrete Fracture and
810   Continuum Models to Predict Contaminant Transport in Fractured Porous Media.
811   Groundwater, 52(1), 84-95.

812   Chen, W., Ghaith, A., Park, A., Ortoleva, P., 1990. Diagenesis through coupled processes:
813   Modeling approach, self-organization, and implications for exploration. In: Meshri, I.,
814   Ortoleva, P. (Eds.), AAPG Memoir 49: Prediction of Reservoir Quality through Chemical
815   Modeling, pp. 103-130.

816   Diersch, H.-J. G., 2002. FEFLOW Finite-Element Subsurface Flow and Transport
817   Simulation System, User's Manual, Release 6.0. WASY GmbH, Berlin, 2002.

818   Diersch, H.J.G., Kolditz, O., 2002. Variable-density flow and transport in porous media:
819   approaches and challenges. Advances in Water Resources, 25(8–12), 899-944.

820   Eckstein, Y., Simmonsi, G., 1977. Measurement and interpretation of terrestrial heat
821   flow in Israel. Geothermics, 6(3–4), 117-142.

822   Evans, D.G., Nunn, J.A., Hanor, J.S., 1991. Mechanisms driving groundwater flow near
823   salt domes. Geophysical Research Letters, 18(5), 927-930.

824   Flexer, A., 1964. The paleogeography of the Senonian and Maestrichtian in northern
825   Israel. PhD Thesis, Hebrew University, Jerusalem, 157 pp.

826   Garven, G., Bull, S.W., Large, R.R., 2001. Hydrothermal fluid flow models of stratiform
827   ore genesis in the McArthur Basin, Northern Territory, Australia. Geofluids, 1(4), 289-311.

828   Gat, J.R., Mazor, E., Tzur, Y., 1969. The stable isotope composition of mineral waters in
829   the Jordan Rift Valley, Israel. Journal of Hydrology, 7(3), 334-352.

830   Goldshmidt, M.J., Arad, A., Neev, D., 1967. The mechanism of the saline springs in the
831   Lake Tiberias depression. Geological Survey of Israel Bulletin, 45, 1-19.

832   Greitzer, Y., 1980. Hydrodynamic Investigation of Geological Formations in Israel for the
833   Purpose of Oil Exploration: Stage 1. Geological and Hydrological Projects.

835   Gvirtzman, H., Garven, G., Gvirtzman, G., 1997a. Hydrogeological modeling of the saline
836   hot springs at the Sea of Galilee, Israel. Water Resources Research, 33(5), 913-926.

837   Gvirtzman, H., Garven, G., Gvirtzman, G., 1997.b Thermal anomalies associated with
838   forced and free ground-water convection in the Dead Sea rift valley. Geological Society of
839   America Bulletin, 109(9), 1167-1176.

840   Hirsch, F., 2005. The Jurassic of Israel. In: J.K. Hall, V.A. Krasheninnikov, F. Hirsch, C.
841   Banjamini, A. Flexer (Ed.), Geological Framework of the Levant, The Levantine Basin and
842   Israel, vol. II, Historical Productions-Hall, Jerusalem, pp. 361-391.

843   Hurwitz, S., Goldman, M., Ezersky, M., Gvirtzman, H., 1999. Geophysical (Time Domain
844   Electromagnetic Model) delineation of a shallow brine beneath a freshwater lake, the Sea of
845   Galilee, Israel. Water Resources Research, 35(12), 3631-3638.

846   Hurwitz, S., Stanislavsky, E., Lyakhovsky, V., Gvirtzman, H., 2000a. Transient
847   groundwater-lake interactions in a continental rift: Sea of Galilee, Israel. Geological Society
848   of America Bulletin, 112(11), 1694-1702.

849   Hurwitz, S., Lyakhovsky, V., Gvirtzman, H., 2000b. Transient salt transport modeling of
850   shallow brine beneath a freshwater lake, the Sea of Galilee, Israel. Water Resources
851   Research, 36(1), 101-107.

852   Inbar, N., 2012. The evaporitic subsurface body of Kinnarot Basin - Stratigraphy,
853   structure, geohydrology. Ph.D Thesis, Tel Aviv University, 131 pp.

854   Ingebritsen, S.E., Sanford, W.E., 1999. Groundwater in geologic processes. Cambridge
855   University Press.

856   Kaudse, T., 2014. Noble gases in groundwater of the Azraq Oasis, Jordan, and along the
857   central Dead Sea Transform - Two case studies Ruperto-Carola University of Heidelberg,
858   Heidelberg 219 pp.

859   Kesler, A., 2011. Hydrological analysis of salt flow into Lake Kinneret. Environmental &
860   Water Resources Engineering (2002) report, (in Hebrew), 61 pp.

861   Klein-BenDavid, O., Sass, E., Katz, A., 2004. The evolution of marine evaporitic brines in
862   inland basins: The Jordan–Dead Sea Rift valley. Geochimica et Cosmochimica Acta, 68(8),
863   1763–1775.

864   Kolodny, Y., Katz, A., Starinsky, T., Moise, T., Simon, E., 1999. Chemical tracing of salinity
865   sources in Lake Kinneret (Sea of Galilee), Israel. Limnol. Oceanogr., 44, 1035-1044.

866   Lapwood, E.R., 1948. Convection of a fluid in a porous medium. Mathematical
867   Proceedings of the Cambridge Philosophical Society, 44(04), 508-521.

868   Levitte, D., Eckstein, Y., 1978. Correlation between the silica concentration and the
869   orifice temperature in the warm springs along the jordan-dead sea rift valley. Geothermics,
870   7(1), 1-8.

871   Lopez, D.L., Smith, L., 1996. Fluid flow in fault zones: influence of hydraulic anisotropy
872   and heterogeneity on the fluid flow and heat transfer regime. Water Resour Res 32:3227–
873   3235

874   Magri, F., Bayer, U., Maiwald, U., Otto, R., Thomsen, C., 2009. Impact of transition zones,
875   variable fluid viscosity and anthropogenic activities on coupled fluid-transport processes in
876   a shallow salt-dome environment. Geofluids, 9(3), 182-194.

877   Magri, F., Akar, T., Gemici, U., Pekdeger, A., 2012. Numerical investigations of fault-
878   induced seawater circulation in the Seferihisar-Balçova Geothermal system, western Turkey.
879   Hydrogeology Journal, 20(1), 103-118.

880   Makhlouf, I., Abu-Azzam, H., Al-Hiayri, A., 1996. Surface and subsurface lithosratigraphic
881   relationships of the Cretacceous Ajlun Group in Jordan. Subsurface Geology Bolletin No.8,
882   95 pp.

883   Marcus, E., Slager , J., 1985. The sedimentary-magmatic sequence of the Zemah-1 well
884   (Jordan-Dead Sea Rift, Israel) and its emplacement in time and space,. Isr. J. Earth Sci., 34, 1-
885   10.

886   Mazor, E., Mero, F., 1969. Geochemical tracing of mineral and fresh water sources in
887   the Lake Tiberias Basin, Israel. Journal of Hydrology, 7(3), 276-317.
888   McCaffrey M.A., Lazar B., Holland HD, 1987. The evaporation path of seawater and the
889   coprecipitation of Br⁻ and K⁺ with halite. Journal of Sedimentary Petrology, 57, 928–937.
890   McKibbin, R., 1986. Heat transfer in a vertically-layered porous medium heated from
891   below. Transp Porous Med, 1(4), 361-370.
892   Meiler, M., 2011. The Deep Geological Structure of the Golan Heights and the Evolution
893   of the Adjacent Dead Sea Fault System. Ph.D Thesis, Tel Aviv University, 153 pp.
894   Mero, F., S. Mandel, 1963. The hydrological mechanism of the saline springs of the
895   western shore of Lake Kinneret (in Hebrew), Rep. 2399, Tahal, Tel-Aviv, 10 pp.
896   Moise, T., Starinsky, A., Katz, A., Kolodny, Y., 2000. Ra isotopes and Rn in brines and
897   ground waters of the Jordan-Dead Sea Rift Valley: enrichment, retardation, and mixing.
898   Geochimica et Cosmochimica Acta, 64, 2371-2388.
899   Möller, P., Siebert, C., Geyer, S., Inbar, N., Rosenthal, E., Flexer, A., Zilberbrand, M.,
900   2012. Relationship of brines in the Kinnarot Basin, Jordan-Dead Sea Rift Valley. Geofluids,
901   12(2), 166-181.
902   Möller, P., Rosenthal, E., Flexer, A., 2014. The hydrogeochemistry of subsurface brines
903   in and west of the Jordan–Dead Sea Transform fault. Geofluids, 14(3), 291-309.
904   Nield, D.A., 1968. Onset of Thermohaline Convection in a Porous Medium. Water
905   Resources Research, 4(3), 553-560.
906   O'Brien J. J., Lerche I., 1988. Impact of Heat Flux around Salt Diapirs and Salt Sheets in
907   the Gulf Coast on Hydrocarbon Maturity: Models and Observations, Gulf Coast Association
908   of Geological Societies Transactions, 38, pp 231–243.
909   Reznikov, M., Ben-Avraham, Z., Garfunkel, Z., Gvirtzman, H., Rotsteina, Y., 2004
910   Structural and stratigraphic framework of Lake Kinneret. Israel Journal of Earth Sciences
911   Volume 53(3-4), 131-149.
912   Rimmer, A., Hurwitz, S., Gvirtzman, H., 1999. Spatial and temporal characteristics of
913   saline springs: Sea of Galilee, Israel. Ground water, 37(5), 663-73.
914   Rimmer, A., 2000. The influence of lake level on the discharge of the Kinneret saline
915   springs. Advances in Limnology, 55(55–67).
916   Rimmer, A., 2003. The mechanism of Lake Kinneret salinization as a linear reservoir.
917   Journal of Hydrology, 281(3), 173-186.
918   Roded, R., Shalev, E., Katoshevski, D., 2013. Basal heat-flow and hydrothermal regime
919   at the Golan–Ajloun hydrological basins. Journal of Hydrology, 476(0), 200-211.
920   Rosenfeld, A., Hirsch, F., 2005. The Cretaceous of Israel. In: Hall J. K., K.V.A., Hirsch F.,
921   Benjamini Ch, Flexer A. (Ed.), Geological Framework of the Levant (II): The Levantine Basin
922   and Israel. Historical Productions, Hall Publications, Jerusalem, Israel, pp. 393-436.
923   Saltzman, U., 1964. The Geology of Tabcha-Hukok-Migdal region. P.N. 374, Tahal, Tel
924   Aviv.
925   Sarkar, A., Nunn, J.A., Hanor, J.S., 1995. Free thermohaline convection beneath
926   allochthonous salt sheets: An agent for salt dissolution and fluid flow in Gulf Coast
927   sediments. Journal of Geophysical Research: Solid Earth 100(B9), 18085-18092.
928   Severini, A.P., Huntley, D., 1983. Heat Convection in Warm Springs Valley, Virginia.
929   Ground Water, 21(6), 726-732.
930   Shalev, E., Lyakhovsky, V., Yechieli, Y., 2007. Is advective heat transport significant at
931   the Dead Sea basin? Geofluids, 7(3), 292-300.
932   Shalev, E., Levitte, D., Gabay, R., Zemach, E., 2008. Assessment of Geothermal Resources
933   in Israel, the Ministry of National Infrastructures Geological Survey of Israel Jerusalem.
934   Shalev, E., Lyakhovsky, V., Weinstein, Y., Ben-Avraham, Z., 2013. The thermal structure
935   of Israel and the Dead Sea Fault. Tectonophysics, 602(0), 69-77.
936   Shewchuk, J.R., 1996. Triangle: Engineering a 2D Quality Mesh Generator and Delaunay
937   Triangulator. In: Lin, M.C., Manocha, D. (Eds.), Applied Computational Geometry: Towards
938   Geometric Engineering. Springer-Verlag, Berlin, pp. 203-222.

939   Shulman, H., Reshef, M., Ben-Avraham, Z., 2004. The structure of the Golan Heights and
940   its tectonic linkage to the Dead Sea Transform and the Palmyrides folding Isr. J. Earth Sci.,
941   53, 225-237.
942   Siebert, C., Möller, P., Geyer, S., Kraushaar, S., Dulski, P., Guttman, J., Subah, A., Rödiger,
943   T., 2014. Thermal waters in the Lower Yarmouk Gorge and their relation to surrounding
944   aquifers. Chemie der Erde - Geochemistry, 74, 425-441.
945   Simmons, C.T., Sharp, J.M., Jr, Nield D.A., 2008. Modes of free convection in fractured
946   low-permeability media. Water ResourRes, 44, W03431.
947   Simon, E., Mero, F., 1992. The salinization mechanism of Lake Kinneret. Journal of
948   Hydrology, 138(3–4), 327-343.
949   Stiller, M., Carmi, I., Münnich, K.O., 1975. Water transport through Lake Kinneret
950   sediments traced by tritium. Earth and Planetary Science Letters, 25(3), 297-304.
951   Stiller, M., Rosenbaum, J.M., Nishri, A., 2009. The origin of brines underlying Lake
952   Kinneret. Chemical Geology, 262(3–4), 293-309.
953   Tsur, N., 2013. Noble gas isotopic signatures in thermal waters of the Dead Sea
954   Transform, Israel, Ruprecht-Karls-University Heidelberg, Heidelberg, 108 pp.
955   Vengosh, A., Rosenthal, E., 1994. Saline groundwater in Israel: its bearing on the water
956   crisis in the country. Journal of Hydrology, 156(1–4), 389-430.
957   Vujević, K., Graf, T., Simmons, C.T., Werner, A.D., 2014. Impact of fracture network
958   geometry on free convective flow patterns. Advances in Water Resources, 71(0), 65-80.
959   Water Authority of Israel, Hydrological Service, 2012. Development of water
960   exploitation and the state of water resources in Israel, Autumn 2011 (in Hebrew), 473 pp.
961   Yang, J., 2006. Finite element modeling of transient saline hydrothermal fluids in
962   multifaulted sedimentary basins: implications for ore-forming processes. Canadian Journal
963   of Earth Sciences, 43(9), 1331-1340.
964   Yechieli Y., Shaliv G., Wallman S., Kessler A., Rozenzpet M., Berger D., Bein A. 2011.
965   Three dimensional model for the Kalanit Basin (Fuliya and Tabgha basin). GSI Project report
966   GSI/38/2011, (in Hebrew), 101 pp.